IEEE Access
Multidisciplinary ⋮ Rapid Review ⋮ Open Access Journal

Received April 23, 2021, accepted May 10, 2021, date of publication May 25, 2021, date of current version June 4, 2021.

Digital Object Identifier 10.1109/ACCESS.2021.3083555

Harmonic Compensation by Limit Cycle Model Predictive Control

CARLOS CATERIANO YÁÑEZ[1,2,3], GERWALD LICHTENBERG[2], GEORG PANGALOS[1], AND JAVIER SANCHIS SÁEZ[3]

[1]Fraunhofer Institute for Wind Energy Systems IWES, 27572 Bremerhaven, Germany
[2]Faculty Life Sciences, Hamburg University of Applied Sciences, 21033 Hamburg, Germany
[3]Instituto Universitario de Automática e Informática Industrial, Universitat Politècnica de València, 46022 Valencia, Spain

Corresponding author: Carlos Cateriano Yáñez (carlos.cateriano.yanez@iwes.fraunhofer.de)

This work was supported in part by the Fraunhofer Institute for Silicon Technology ISIT within the Project NEW 4.0 (North German Energy Transition 4.0), which is funded by the German Bundesministerium für Wirtschaft und Energie (BMWi), and in part by the Free and Hanseatic City of Hamburg.

ABSTRACT This work develops a novel limit cycle model predictive controller aimed at harmonic compensation. The proposed nonlinear controller embeds the dynamics of a circular limit cycle of a supercritical Neimark-Sacker normal form directly into its cost function. This enables the controller to steer the state dynamics into a fundamental harmonic shape in systems where a periodic solution is desired. The proposed cost function structure is analyzed for possible convex formulations that could lead to more effective methods for solving the optimization problem. A simulation study in the field of electric power systems integrated with renewable energy resources is given. The new controller is used to set the reference of the compensation current of an active power filter to address the harmonic distortion in the grid. The results show that the controller can mitigate the harmonic disturbance content in voltages and currents to the required levels while maintaining the correct amplitudes at the desired fundamental frequency.

INDEX TERMS Predictive control, nonlinear systems, limit-cycles, optimization, convex functions.

I. INTRODUCTION

Harmonic compensation is important for various fields, of which two come to mind immediately. The absence of frequencies in vibrations of mechanical systems, especially the resonance frequency, is as interesting as the absence of oscillations in electrical systems other than the fundamental frequency.

In the operation of electrical grids, harmonic compensation plays a crucial role in power quality improvements. Different approaches exist of which most are associated with active power filters (APFs), particularly shunt active power filters (SAPFs). To control SAPFs, the quasi-standard is to use instantaneous symmetrical component (ISC), instantaneous reactive power (IRP) (also known as pq) in the α-β domain, or synchronous reference frame (SRF) in the $dq0$ reference frame, to generate the reference compensation current, typically paired with a low-pass filter (LPF) and a proportional–integral (PI) controller [1]–[3].

The associate editor coordinating the review of this manuscript and approving it for publication was Di He.

For selective harmonic compensation, performance can be improved with proportional–integral resonant (PI-R) controllers instead, as seen in [4]. More advanced approaches proposed the control of distributed generation sources by use of parallel control of the voltage amplitude and harmonic compensation, [5], or by hierarchical control, [6]. However, selective approaches increase in computation complexity as more harmonics are considered since each requires an individual controller, [7]. For non-selective harmonic compensation, which is the aim of the proposed method, the most widely used among the advanced control schemes are repetitive control (RC), sliding mode control (SMC), and predictive control, [7].

Repetitive control, although originally proposed for the control of a proton synchrotron [8], was developed in numerous papers over the last years for the control of APFs. In [9] a repetitive controller was proposed, which compensates selected current harmonics. A special feedback structure was designed for power electronic applications in [10]. A plug-in discrete-time repetitive algorithm for current-harmonic compensation was proposed in [11], where detailed design, analysis, and application of the controller can be found. In [12]

an approach of a digital repetitive plug-in controller for odd-harmonic discrete-time periodic references and disturbances was proposed, which does not introduce a high gain at frequencies for which it is not needed, therefore improving robustness. A different approach to reducing the gain at high frequencies was reported in [13]. Repetitive control algorithms which can cope with varying frequency of the periodic signal were proposed in [14]–[16]. To reduce the computational effort [17] proposed a controller with an inner PI control loop running at a sampling rate identical to switching frequency and an external plug-in repetitive control loop with a reduced sampling rate.

The concept of SMC emerges from the study of variable structure control systems pioneered at the Russian Institute of Control Sciences starting in the late 1960s, [18], [19]. The first implementations for APFs started in the 1990's, [20]. Due to its robustness towards disturbances and parameter variations, the method has been widely adopted. However, the chattering caused by its large switching gain can lead to instability, hindering power quality. To reduce the chattering phenomena, an integral sliding mode control (ISMC) approach that focuses only on the harmonic components and uses a boundary layer as a switching function is proposed in [21]. More recently, in [22], a complementary sliding surface is introduced to further reduce chattering and increase accuracy, alongside an adaptive backstepping radical basis function neuronal network estimator for disturbances.

In the case of predictive control for SAPF, approaches using a deadbeat model predictive control (DBMPC) scheme to ensure fast dynamics and high accuracy have been proposed in [23], [24]. Regarding selective harmonic compensation, in the field of vibration control, the proposed control techniques range from standard linear quadratic regulator (LQR) controllers up to model-based approaches as given in [25] where a nonlinear model predictive control (NMPC) is used with constraints to ensure the absence of specific frequencies in the output of a system.

This work proposes a Limit cycle model predictive control (LCMPC), a new NMPC approach aimed towards systems with periodic dynamics where a single fundamental frequency at a specific amplitude is desired. The LCMPC aims to leverage the target system's periodic behavior for its predictions while using the attractor dynamics of a stable circular limit cycle to ensure a fundamental harmonic shape of the targeted states at a specific amplitude and frequencies. The potential of the limit cycle dynamics has already been proven for other grid applications, e.g., the dVOC for grid-forming from [26], where a Van der Pol oscillator is used.

Initial research on the LCMPC was presented in [27], where an overview of the basic components of the control principle and some early results were shown. The present work aims at considerably extending this previous contribution by including more in-depth analysis and development of the control principle, giving a more exhaustive theory foundation. These extensions will be further detailed in the following paper structure overview.

Starting at Section II, this section extends on the previous contribution giving the required proofs behind the formulation of the supercritical Neimark-Sacker bifurcation normal form used by the controller, as well as a detailed analysis of the critical points of the radius governed by these dynamics. Section III gives the full derivation of the LCMPC cost function formulation and a detailed proof of its connection to the limit cycle dynamics. In Section IV, a convexity analysis of the cost function is added, where the current research paths in this aspect are explored. Section V presents a more exhaustive analysis of the previous APF application example, where more detailed results are given, including an additional convexity numerical test and a qualitative comparison against other control approaches. Finally, Section VI draws the concluding remarks that bring together the LCMPC analysis while setting up the future research directions.

II. LIMIT CYCLE FOR MAPS

The proposed controller relies on the dynamics of discrete-time systems where a periodic behavior can arise, namely a limit cycle (see Appendix A).

A. NEIMARK-SACKER BIFURCATION NORMAL FORM

A particular limit cycle case for maps is given as follows. Consider the normal form of the Neimark-Sacker bifurcation in polar coordinates

$$r_{k+1} = r_k + \mu r_k + \alpha r_k^3, \tag{1a}$$
$$\theta_{k+1} = \theta_k + \phi, \tag{1b}$$

with parameters $\{\mu, \alpha, \phi\} \in \mathbb{R}$, in discrete time $k \in \mathbb{Z}$, with sampling time $\tau = \frac{t}{k}$, [28].

A system transformation to analyze the phase-space dynamics is proposed as follows.

Proposition 1: The phase space of the normal form in (1) is described by the second-order discrete-time system in Cartesian coordinates

$$\mathbf{x}_{k+1} = \left(1 + \mu + \alpha \mathbf{x}_k^\mathsf{T} \mathbf{x}_k\right) \mathbf{R}_\phi \mathbf{x}_k, \tag{2}$$

where

$$\mathbf{x} = \begin{bmatrix} x_1 & x_2 \end{bmatrix}^\mathsf{T}, \tag{2a}$$
$$\mathbf{R}_\phi = \begin{bmatrix} \cos(\phi) & -\sin(\phi) \\ \sin(\phi) & \cos(\phi) \end{bmatrix}. \tag{2b}$$

Proof: Let the transformation from polar to Cartesian coordinates be given by

$$x_1 = r\cos(\theta), \tag{3a}$$
$$x_2 = r\sin(\theta). \tag{3b}$$

From (3) it follows that

$$r = \sqrt{x_1^2 + x_2^2}, \tag{4a}$$
$$\theta = \arctan\left(\frac{x_2}{x_1}\right). \tag{4b}$$

Replacing (4) in (1) leads to

$$r_{k+1} = \sqrt{x_{1,k}^2 + x_{2,k}^2}\left(1 + \mu + \alpha\left(x_{1,k}^2 + x_{2,k}^2\right)\right), \quad (5a)$$

$$\theta_{k+1} = \arctan\left(\frac{x_{2,k}}{x_{1,k}}\right) + \phi. \quad (5b)$$

Given the trigonometric identities

$$\sin(a \pm b) = \sin(a)\cos(b) \pm \cos(a)\sin(b), \quad (6a)$$

$$\cos(a \pm b) = \cos(a)\cos(b) \mp \sin(a)\sin(b), \quad (6b)$$

expressing the Cartesian coordinates transformation in (3) in terms of (5) and applying the identities in (6) results on

$$x_{1,k+1} = \left(1+\mu+\alpha\left(x_{1,k}^2 + x_{2,k}^2\right)\right)\left(x_{1,k}\cos(\phi) - x_{2,k}\sin(\phi)\right), \quad (7a)$$

$$x_{2,k+1} = \left(1+\mu+\alpha\left(x_{1,k}^2 + x_{2,k}^2\right)\right)\left(x_{2,k}\cos(\phi) + x_{1,k}\sin(\phi)\right). \quad (7b)$$

Finally, rearranging (7) into vector form using (2a) and (2b) for factorization leads to (2). □

B. SUPERCRITICAL NEIMARK-SACKER BIFURCATION

A particular case of the Neimark-Sacker bifurcation is defined as follows.

Definition 1: When $\mu > 0$, $\alpha < 0$ and $\phi > 0$, the normal form in (1) undergoes a supercritical Neimark-Sacker bifurcation, leading to an unstable fixed point at the origin and a stable unique circular limit cycle surrounding it, [29].

A supercritical Neimark-Sacker bifurcation with a unique circular limit cycle of radius one can be observed in Fig. 1. The red arrows denote the vector field that describes the dynamics of the system as given in (2). It can be observed that the system trajectories tend towards the circular limit cycle centered around the origin. As an example, five trajectories starting along the line $x_1 = x_2$ are shown. The blue-filled circles denote the starting point of the trajectories, while the solid blue lines show the evolution of their trajectories, with blue dots markings their discrete steps and arrows pointing their direction. The trajectories starting around the limit cycle are attracted towards it. However, this is not the case for the one at the origin, which remains at that unstable fixed point.

From the system parameters, the radius of the circular limit cycle can be calculated as follows.

Proposition 2: The radius of the unique stable circular limit cycle of the supercritical Neimark-Sacker normal form from Definition 1 for (1) is given by

$$\rho = \sqrt{-\frac{\mu}{\alpha}}. \quad (8)$$

Proof: Replacing r_k by ρ in (1a) leads to

$$r_{k+1} = \sqrt{-\frac{\mu}{\alpha}}. \quad (9)$$

□

Depending on the trajectory initial conditions, further critical points can be identified.

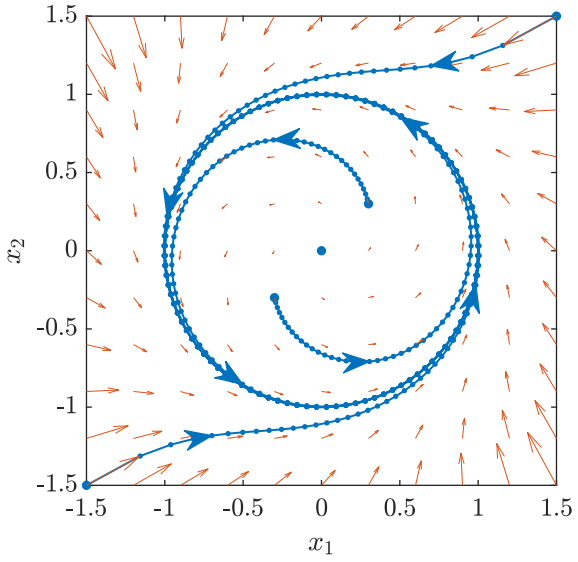

FIGURE 1. Supercritical Neimark-Sacker bifurcation normal form phase portrait with $\mu = 0.05$, $\alpha = -0.05$, $\tau = 0.2$ ms, and $\phi = 2\pi 50\tau$.

Proposition 3: Trajectories starting at a radius of

$$\rho_0 = \sqrt{-\frac{(1+\mu)}{\alpha}}, \quad (10)$$

of the supercritical Neimark-Sacker normal form from Definition 1 for (1), lead to the unstable fixed point at the origin.

Proof: Replacing r_k by ρ_0 in (1a) leads to

$$r_{k+1} = 0. \quad (11)$$

□

Proposition 4: Trajectories starting at a radius greater than

$$\rho_\infty = \sqrt{-\frac{(2+\mu)}{\alpha}}, \quad (12)$$

of the supercritical Neimark-Sacker normal form from Definition 1 for (1), will diverge in magnitude towards ∞.

Proof: Let

$$r_k = \rho_\infty + \epsilon, \quad (13)$$

where $\epsilon > 0$. Replacing (13) in (1a), leads to

$$r_{k+1} = (\rho_\infty + \epsilon)\left(-1 + 2\alpha\epsilon\rho_\infty + \alpha\epsilon^2\right). \quad (14)$$

From Definition 1 it follows that $\alpha < 0$, thus

$$r_{k+1} = -(\rho_\infty + \epsilon)\left(1 + 2|\alpha|\epsilon\rho_\infty + |\alpha|\epsilon^2\right). \quad (15)$$

Therefore $|r_{k+1}| > |r_k|$, where $|r_{k+1}| - |r_k|$ increases as the discrete time $k \to \infty$, thus $|r| \to \infty$. □

Fig. 2 shows the iterative evolution of the radius map as given by (1a) at different starting points for $\mu = 0.05$ and $\alpha = -0.05$. The critical points: $|\rho|$, $|\rho_0|$, and $|\rho_\infty|$; are represented by the markers: asterisk, square, and circle, correspondingly. The behavior observed agrees with the analysis done in the previous propositions for each critical point.

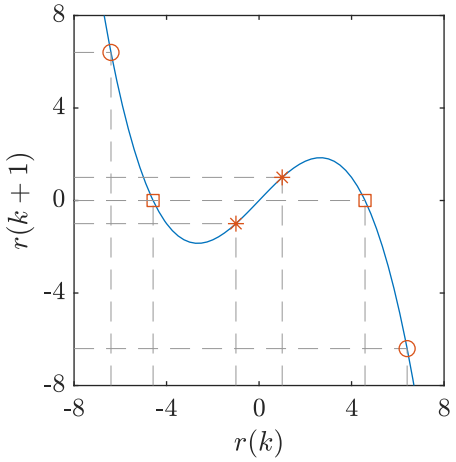

FIGURE 2. Supercritical Neimark-Sacker bifurcation normal form radius map evolution with $\mu = 0.05$ and $\alpha = -0.05$.

Radius starting points with magnitudes below ρ_0 will tend towards ρ, points with a magnitude between ρ_0 and ρ_∞ will also tend towards ρ but alternate in sign, and points with a magnitude greater than ρ_∞ will diverge.

This behavior is also observed in Fig. 1, which uses the same parameters, where the region of attraction surrounding the circular limit cycle ensures that all neighboring trajectories lead to it. Therefore, once the states reach the limit cycle, they will remain in this periodic orbit with a fundamental harmonic shape of radius ρ and angular frequency $\omega = \frac{\phi}{\tau}$, see (3). These dynamics are the foundation of the proposed controller cost function, as shown in Section III.

III. LIMIT CYCLE MODEL PREDICTIVE CONTROL

This section comprises the different building blocks of the proposed LCMPC approach. The objective of the controller design is to embed the dynamics of the circular limit cycle explored in Section II within its control law.

A. COST FUNCTION KERNEL FORMULATION

Typically, a model predictive control (MPC) relies on the minimization of a cost function $J \in \mathbb{R}$ over a finite prediction horizon $H_p \in \mathbb{N}$ to calculate its control action, [30]. For the LCMPC, the cost function is defined as

$$J(\mathbf{X}) = \mathbf{X}^\mathsf{T}\mathbf{Q}_2\mathbf{X} + 2\alpha\mathbf{X}^\mathsf{T}\left(\mathbf{L}\circ\left(\mathbf{X}\mathbf{X}^\mathsf{T}\mathbf{Q}_4\right)\right)\mathbf{X} + \alpha^2\mathbf{X}^\mathsf{T}\left(\mathbf{L}\circ\left(\mathbf{X}\mathbf{X}^\mathsf{T}\left(\mathbf{L}\circ\left(\mathbf{X}\mathbf{X}^\mathsf{T}\right)\right)\right)\right)\mathbf{X}, \quad (16)$$

where $\circ$ is the Hadamard product and

$$\mathbf{X} = \begin{bmatrix}\mathbf{x}_{k+1}^\mathsf{T} & \mathbf{x}_{k+2}^\mathsf{T} & \cdots & \mathbf{x}_{k+H_p}^\mathsf{T}\end{bmatrix}^\mathsf{T}, \quad (16a)$$

$$\mathbf{Q}_2 = \begin{bmatrix} (1+\mu)^2\mathbf{I}_{2\times2} & -(1+\mu)\mathbf{R}_\phi^\mathsf{T} & \mathbf{0}_{2\times2} & \cdots \\ -(1+\mu)\mathbf{R}_\phi & \left(1+(1+\mu)^2\right)\mathbf{I}_{2\times2} & \ddots & \ddots \\ \mathbf{0}_{2\times2} & \ddots & \ddots & \ddots \\ \vdots & \ddots & \ddots & \ddots \\ \vdots & \ddots & \ddots & \ddots \\ \vdots & \ddots & \ddots & \ddots \\ \mathbf{0}_{2\times2} & \cdots & \cdots & \cdots \end{bmatrix}$$
$$\begin{bmatrix} \cdots & \cdots & \cdots & \mathbf{0}_{2\times2} \\ \ddots & \ddots & \ddots & \vdots \\ \ddots & \ddots & \ddots & \vdots \\ \ddots & \ddots & \ddots & \vdots \\ \ddots & \ddots & \ddots & \mathbf{0}_{2\times2} \\ \ddots & \ddots & \left(1+(1+\mu)^2\right)\mathbf{I}_{2\times2} & -(1+\mu)\mathbf{R}_\phi^\mathsf{T} \\ \cdots & \mathbf{0}_{2\times2} & -(1+\mu)\mathbf{R}_\phi & \mathbf{I}_{2\times2} \end{bmatrix}, \quad (16b)$$

$$\mathbf{L} = \begin{bmatrix} \mathbf{1}_{2\times2} & \mathbf{0}_{2\times2} & \cdots & \cdots & \mathbf{0}_{2\times2} \\ \mathbf{0}_{2\times2} & \ddots & \ddots & \ddots & \vdots \\ \vdots & \ddots & \ddots & \ddots & \vdots \\ \vdots & \ddots & \ddots & \mathbf{1}_{2\times2} & \mathbf{0}_{2\times2} \\ \mathbf{0}_{2\times2} & \cdots & \cdots & \mathbf{0}_{2\times2} & \mathbf{0}_{2\times2} \end{bmatrix}, \quad (16c)$$

$$\mathbf{Q}_4 = \begin{bmatrix} (1+\mu)\mathbf{I}_{2\times2} & \mathbf{0}_{2\times2} & \cdots & \cdots & \cdots & \mathbf{0}_{2\times2} \\ -\mathbf{R}_\phi & \ddots & \ddots & \ddots & \ddots & \vdots \\ \mathbf{0}_{2\times2} & \ddots & \ddots & \ddots & \ddots & \vdots \\ \vdots & \ddots & \ddots & \ddots & \ddots & \vdots \\ \vdots & \ddots & \ddots & \ddots & (1+\mu)\mathbf{I}_{2\times2} & \mathbf{0}_{2\times2} \\ \mathbf{0}_{2\times2} & \cdots & \cdots & \mathbf{0}_{2\times2} & -\mathbf{R}_\phi & \mathbf{0}_{2\times2} \end{bmatrix}, \quad (16d)$$

with dimensions, $\mathbf{X} \in \mathbb{R}^{2H_p}$, $\mathbf{Q}_2 \in \mathbb{R}^{2H_p\times2H_p}$, $\mathbf{L} \in \mathbb{R}^{2H_p\times2H_p}$, and $\mathbf{Q}_4 \in \mathbb{R}^{2H_p\times2H_p}$; where $\{\mathbf{0}_{j\times j}, \mathbf{1}_{j\times j}, \mathbf{I}_{j\times j}\} \in \mathbb{Z}_{\geq 0}^{j\times j}$ are matrices of zeros, ones, and identity respectively. In this formulation, the future state signals vector $\mathbf{X}$ can be seen as the decision variable of the nonlinear optimization problem

$$\min_{\mathbf{X}} J(\mathbf{X}). \quad (17)$$

Theorem 1: Let

$$\mathbf{X}^\star = \arg\min J, \quad (18)$$

be the solution of the optimization problem in (17)*. If and only if* $J(\mathbf{X}^\star) = 0$*, then the optimal solution vector of future state signals* $\mathbf{X}^\star$ *obeys the discrete-time dynamics of the Neimark-Sacker normal form in* (2)*.*

Proof: Rearranging (2) to the right-hand side leads to the kernel

$$\mathbf{0}_{2\times1} = \mathbf{x}_{k+1} - (1+\mu)\mathbf{R}_\phi\mathbf{x}_k - \alpha\mathbf{R}_\phi\mathbf{x}_k\mathbf{x}_k^\mathsf{T}\mathbf{x}_k. \quad (19)$$

Making a scalar product of the transposed kernel in (19) times itself expands to

$$\begin{aligned}
&\mathbf{x}_{k+1}^{\mathsf{T}}\mathbf{x}_{k+1} - (1+\mu)\,\mathbf{x}_{k+1}^{\mathsf{T}}\mathbf{R}_{\phi}\mathbf{x}_{k} + (1+\mu)^{2}\,\mathbf{x}_{k}^{\mathsf{T}}\mathbf{x}_{k} \\
&\quad - \alpha\mathbf{x}_{k+1}^{\mathsf{T}}\mathbf{R}_{\phi}\mathbf{x}_{k}\mathbf{x}_{k}^{\mathsf{T}}\mathbf{x}_{k} - (1+\mu)\,\mathbf{x}_{k}^{\mathsf{T}}\mathbf{R}_{\phi}^{\mathsf{T}}\mathbf{x}_{k+1} \\
&\quad + \alpha\,(1+\mu)\,\mathbf{x}_{k}^{\mathsf{T}}\mathbf{x}_{k}\mathbf{x}_{k}^{\mathsf{T}}\mathbf{x}_{k} - \alpha\mathbf{x}_{k}^{\mathsf{T}}\mathbf{x}_{k}\mathbf{x}_{k}^{\mathsf{T}}\mathbf{R}_{\phi}^{\mathsf{T}}\mathbf{x}_{k+1} \\
&\quad + \alpha\,(1+\mu)\,\mathbf{x}_{k}^{\mathsf{T}}\mathbf{x}_{k}\mathbf{x}_{k}^{\mathsf{T}}\mathbf{x}_{k} + \alpha^{2}\mathbf{x}_{k}^{\mathsf{T}}\mathbf{x}_{k}\mathbf{x}_{k}^{\mathsf{T}}\mathbf{x}_{k}\mathbf{x}_{k}^{\mathsf{T}}\mathbf{x}_{k}. \qquad (20)
\end{aligned}$$

Stacking the consecutive states in (20) as $\mathbf{Z}_k = \begin{bmatrix}\mathbf{x}_k^{\mathsf{T}} & \mathbf{x}_{k+1}^{\mathsf{T}}\end{bmatrix}^{\mathsf{T}}$, a cost function can be defined as

$$\begin{aligned}
G_k\left(\mathbf{Z}_k\right) = \mathbf{Z}_k^{\mathsf{T}}&\begin{bmatrix}(1+\mu)^{2}\,\mathbf{I}_{2\times2} & -(1+\mu)\,\mathbf{R}_{\phi}^{\mathsf{T}} \\ -(1+\mu)\,\mathbf{R}_{\phi} & \mathbf{I}_{2\times2}\end{bmatrix}\mathbf{Z}_k \\
&+ 2\alpha\mathbf{Z}_k^{\mathsf{T}}\mathbf{L}_0\mathbf{Z}_k\mathbf{Z}_k^{\mathsf{T}}\begin{bmatrix}(1+\mu)\,\mathbf{I}_{2\times2} & \mathbf{0}_{2\times2} \\ -\mathbf{R}_{\phi} & \mathbf{0}_{2\times2}\end{bmatrix}\mathbf{Z}_k \\
&+ \alpha^{2}\mathbf{Z}_k^{\mathsf{T}}\mathbf{L}_0\mathbf{Z}_k\mathbf{Z}_k^{\mathsf{T}}\mathbf{L}_0\mathbf{Z}_k\mathbf{Z}_k^{\mathsf{T}}\mathbf{L}_0\mathbf{Z}_k, \qquad (21)
\end{aligned}$$

where

$$\mathbf{L}_0 = \begin{bmatrix}\mathbf{I}_{2\times2} & \mathbf{0}_{2\times2} \\ \mathbf{0}_{2\times2} & \mathbf{0}_{2\times2}\end{bmatrix}. \qquad (21a)$$

This cost function quantifies the squared error of two consecutive states with respect to the normal form dynamics from (2), thus defining a nonlinear shape residual. This expression can be extended from time $k+1$ up to the whole prediction horizon H_p by a consecutive sum of the squared error expression in (21), such that

$$\sum_{n=k+1}^{k+H_p} G_n\left(\mathbf{Z}_n\left(\mathbf{X}\right)\right) = J\left(\mathbf{X}\right), \qquad (22)$$

where

$$\mathbf{Z}_n\left(\mathbf{X}\right) = \begin{bmatrix}\mathbf{0}_{4\times2(n-k-1)} & \mathbf{I}_{4\times4} & \mathbf{0}_{4\times2\left(k+H_p-1-n\right)}\end{bmatrix}\mathbf{X}, \qquad (22a)$$

is an affine vector function in $\mathbf{X}$ that reduces the future state vector to only two consecutive state predictions. This formulation is the expanded form of (16).

If and only if $J\left(\mathbf{X}^{\star}\right) = 0$, then every summand in (22) is $G_n\left(\mathbf{Z}_n\left(\mathbf{X}^{\star}\right)\right) = 0$, since it is a sum of squared errors. Therefore, for any pair of consecutive states in $\mathbf{X}^{\star}$ for $n = k$, given as $\mathbf{Z}_{n=k}\left(\mathbf{X}^{\star}\right) = \mathbf{Z}_k^{\star}$, the nonlinear shape residual in (21) is $G_k\left(\mathbf{Z}_k^{\star}\right) = 0$; thus following the dynamics of (2) since the right-hand side of (19) is also zero. □

B. LINEAR SYSTEM PREDICTIONS

The proposed cost function in (16) enforces the dynamics of the autonomous nonlinear system in (2) onto a set of future state signals $\mathbf{X}$. These future state signals, in a predictive control setup, will belong to the dynamics of a target system, which will be steered by the controller input. For this approach, the target system is assumed to be linear, with dynamics defined as follows.

Definition 2: The dynamics of a discrete-time linear system are given by the state-space equations

$$\mathbf{x}_{k+1} = \mathbf{A}\mathbf{x}_k + \mathbf{B}\mathbf{u}_k + \mathbf{F}\mathbf{v}_k, \qquad (23a)$$
$$\mathbf{y}_k = \mathbf{C}\mathbf{x}_k + \mathbf{w}_k, \qquad (23b)$$

with state vector $\mathbf{x} \in \mathbb{R}^n$, control input $\mathbf{u} \in \mathbb{R}^m$, measured input disturbance $\mathbf{v} \in \mathbb{R}^d$, output $\mathbf{y} \in \mathbb{R}^r$, output disturbance $\mathbf{w} \in \mathbb{R}^r$, system matrix $\mathbf{A} \in \mathbb{R}^{n\times n}$, input matrix $\mathbf{B} \in \mathbb{R}^{n\times m}$, measured input disturbance matrix $\mathbf{F} \in \mathbb{R}^{n\times d}$, and output matrix $\mathbf{C} \in \mathbb{R}^{r\times n}$.

Therefore, for a digital controller such as the MPC, the discrete-time linear system in (23a), can be used to iteratively formulate the future state trajectories $\hat{\mathbf{x}}$ up to a prediction horizon of H_p in terms of the future control input sequence $\hat{\mathbf{u}}$. From now on, the hat symbol $\hat{}$ above a signal denotes that it is a prediction.

Assuming an initial state vector $\mathbf{x}_k$ and a prediction for the future measured input disturbances $\hat{\mathbf{v}}$, [30]; the linear system prediction equations can be formulated as

$$\mathbf{X}\left(\mathbf{U}\right) = \Psi\mathbf{x}_k + \Theta\mathbf{U} + \Gamma\mathbf{V}, \qquad (24)$$

where

$$\mathbf{X} = \begin{bmatrix}\hat{\mathbf{x}}_{k+1}^{\mathsf{T}} & \cdots & \hat{\mathbf{x}}_{k+H_p}^{\mathsf{T}}\end{bmatrix}^{\mathsf{T}} \in \mathbb{R}^{nH_p}, \qquad (24a)$$

$$\Psi = \begin{bmatrix}\mathbf{A}^{\mathsf{T}} & \left(\mathbf{A}^{2}\right)^{\mathsf{T}} & \cdots & \left(\mathbf{A}^{H_p}\right)^{\mathsf{T}}\end{bmatrix}^{\mathsf{T}} \in \mathbb{R}^{nH_p\times n}, \qquad (24b)$$

$$\Theta = \begin{bmatrix}\mathbf{B} & \mathbf{0}_{r\times m} & \cdots & \mathbf{0}_{r\times m} \\ \mathbf{AB} & \mathbf{B} & \cdots & \mathbf{0}_{r\times m} \\ \vdots & \vdots & \ddots & \vdots \\ \mathbf{A}^{H_p-1}\mathbf{B} & \mathbf{A}^{H_p-2}\mathbf{B} & \cdots & \mathbf{B}\end{bmatrix} \in \mathbb{R}^{nH_p\times mH_p}, \qquad (24c)$$

$$\mathbf{U} = \begin{bmatrix}\hat{\mathbf{u}}_k^{\mathsf{T}} & \cdots & \hat{\mathbf{u}}_{k+H_p-1}^{\mathsf{T}}\end{bmatrix}^{\mathsf{T}} \in \mathbb{R}^{mH_p}, \qquad (24d)$$

$$\Gamma = \begin{bmatrix}\mathbf{F} & \mathbf{0}_{r\times d} & \cdots & \mathbf{0}_{r\times d} \\ \mathbf{AF} & \mathbf{F} & \cdots & \mathbf{0}_{r\times d} \\ \vdots & \vdots & \ddots & \vdots \\ \mathbf{A}^{H_p-1}\mathbf{F} & \mathbf{A}^{H_p-2}\mathbf{F} & \cdots & \mathbf{F}\end{bmatrix} \in \mathbb{R}^{nH_p\times dH_p}, \qquad (24e)$$

$$\mathbf{V} = \begin{bmatrix}\hat{\mathbf{v}}_k^{\mathsf{T}} & \cdots & \hat{\mathbf{v}}_{k+H_p-1}^{\mathsf{T}}\end{bmatrix}^{\mathsf{T}} \in \mathbb{R}^{dH_p}. \qquad (24f)$$

By constraining the solution space of the optimization problem in (17) with these linear system prediction equations, the decision variable changes to the future control input $\mathbf{U}$ as

$$\min_{\mathbf{U}}\ J\left(\mathbf{X}\left(\mathbf{U}\right)\right), \qquad (25)$$
$$\text{s.t. } \mathbf{X}\left(\mathbf{U}\right) = \Psi\mathbf{x}_k + \Theta\mathbf{U} + \Gamma\mathbf{V}, \qquad (25a)$$

thus aligning the optimization problem solution with the controller action via $\mathbf{U}$ and reducing the phase space to the target system dynamics embedded in (25a).

C. INPUT FOURIER APPROXIMATION

The LCMPC objective is to ensure that the target system state signals have a fundamental harmonic shape, thus compensating for any harmonic distortion in them. In this context, it is assumed that the future control input sequence $\hat{\mathbf{u}}$ is periodic and therefore can be approximated for a fixed bandwidth up to the h^{th} harmonic by

$$\hat{\mathbf{u}}(k\tau) \approx \sum_{n=1}^{h} \mathbf{f}_n \sin(n\omega k\tau) + \mathbf{g}_n \cos(n\omega k\tau), \tag{26}$$

with Fourier coefficients $\mathbf{f}_n \in \mathbb{R}^m$ and $\mathbf{g}_n \in \mathbb{R}^m$ for the n^{th} harmonic of the fundamental angular frequency ω. Extending this approximation in vector form to match the dimensions of $\mathbf{U}$ in (24d), starting at discrete-time $k = 0$ up to $k = H_p - 1$, leads to

$$\mathbf{U} = (\mathbf{M} \otimes \mathbf{I}_{m\times m})\,\mathbf{P} + \mathcal{O}, \tag{27}$$

where $\otimes$ is the Kronecker product and $\mathcal{O}$ are the higher-order terms the h^{th} harmonic and

$$\mathbf{M} = \begin{bmatrix} 0 & \cdots & 0 \\ \sin(\omega\tau) & \cdots & \sin(h\omega\tau) \\ \vdots & \cdots & \vdots \\ \sin\left(\omega\tau\left(H_p-1\right)\right) & \cdots & \sin\left(h\omega\tau\left(H_p-1\right)\right) \end{bmatrix} \cdots \begin{bmatrix} 1 & \cdots & 1 \\ \cos(\omega\tau) & \cdots & \cos(h\omega\tau) \\ \vdots & \cdots & \vdots \\ \cos\left(\omega\tau\left(H_p-1\right)\right) & \cdots & \cos\left(h\omega\tau\left(H_p-1\right)\right) \end{bmatrix} \in \mathbb{R}^{H_p\times 2h}, \tag{27a}$$

$$\mathbf{P} = \left[\mathbf{f}_1^{\mathsf{T}} \cdots \mathbf{f}_h^{\mathsf{T}} \,|\, \mathbf{g}_1^{\mathsf{T}} \quad \cdots \quad \mathbf{g}_h^{\mathsf{T}}\right]^{\mathsf{T}} \in \mathbb{R}^{2mh}. \tag{27b}$$

Using (27) as a future control input sequence set, a set of future state signals $\breve{\mathbf{X}}$ neglecting $\mathcal{O}$ can be formulated with the linear system predictions in (24) as

$$\breve{\mathbf{X}}(\mathbf{P}) = \Psi\mathbf{x}_k + \Theta(\mathbf{M} \otimes \mathbf{I}_{m\times m})\,\mathbf{P} + \Gamma\mathbf{V}. \tag{28}$$

Assuming that the future control input sequence $\mathbf{U}$ in (25a) is periodic in $\frac{2\pi}{\omega}$ and contains only harmonics up to the h^{th} order, then $\mathbf{X}(\mathbf{U}) = \breve{\mathbf{X}}(\mathbf{P})$.

Following this assumption, the solution space of the decision variable $\mathbf{X}$ in the optimization problem (17) can be further reduced as long as $2mh < mH_p$. In this configuration, $\mathbf{X}$ will be limited to harmonic combinations given by the Fourier coefficients in $\mathbf{P}$ as an input, thus reformulating the optimization problem into

$$\min_{\mathbf{P}} J(\mathbf{X}(\mathbf{P})), \tag{29}$$

$$\text{s.t. } \mathbf{X}(\mathbf{P}) = \Psi\mathbf{x}_k + \Theta(\mathbf{M} \otimes \mathbf{I}_{m\times m})\,\mathbf{P} + \Gamma\mathbf{V}. \tag{29a}$$

This Fourier approximation approach, while restricting the controller action, also can reduce the search space of the optimization solver considerably. Ultimately, it brings a trade-off that will be specific to each application, where the harmonic band upper-limit h will be the tuning parameter.

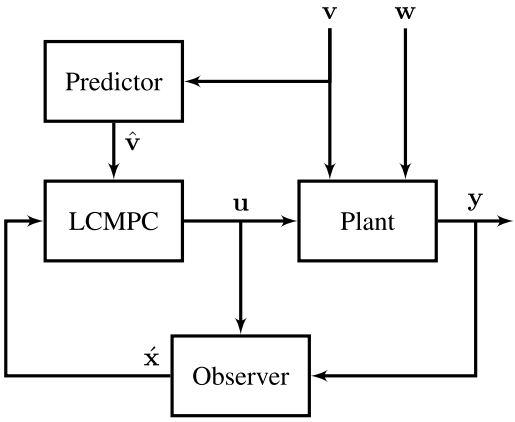

FIGURE 3. Limit cycle model predictive control block diagram.

Finally, Fig. 3 shows the block diagram of the LCMPC considering all the features described throughout this section. The LCMPC block requires two inputs to check the equality constraint in (29a), the state vector estimation $\acute{\mathbf{x}}$ from the observer block and a prediction of the future measured input disturbance $\hat{\mathbf{v}}$ for the next prediction horizon from the predictor block. By finding the optimal $\mathbf{P}^\star$ that solves the minimization problem in (29), the LCMPC block can calculate the optimal input $\mathbf{u}$ using the Fourier parameterization in (27), which then will be provided to the plant block in the next period. The plant block represents the real system, which is expected to follow the linear dynamics introduced in (23). The plant block output measurements $\mathbf{y}$ are then processed by the observer to update the state vector estimation $\acute{\mathbf{x}}$ for the next period, thus closing the control loop.

IV. CONVEXITY ANALYSIS

By looking at the high-order terms of the LCMPC cost function in (16), it can be concluded that the optimization problem posed in (29) is neither a linear programming nor a least-squares problem. However, the possibility that (29) is a convex problem should be investigated because of the effective methods for solving them, [31]. Therefore, a convexity analysis of (29) is carried out in this section.

A. COST FUNCTION DECOMPOSITION

This convexity analysis approach revolves around the following definition.

Definition 3: Let a function $g : \mathbb{R}^m \mapsto \mathbb{R}$ be a composition of the function $f : \mathbb{R}^n \mapsto \mathbb{R}$ with an affine map such that

$$g(\mathbf{x}) = f(\mathbf{A}\mathbf{x} + \mathbf{b}), \tag{30}$$

where $\mathbf{A} \in \mathbb{R}^{n\times m}$, and $\mathbf{b} \in \mathbb{R}^n$; with its domain defined as $\mathbf{dom}\, g = \{\mathbf{x} \,|\, \mathbf{A}\mathbf{x} + \mathbf{b} \in \mathbf{dom}\, f\}$. If f is convex, then g is also convex, [31]

Theorem 2: If the squared kernel cost function $G_k(\mathbf{Z}_k)$ in (21) is convex in $\mathbf{Z}_k$ then the cost function $J(\mathbf{X}(\mathbf{P}))$ of the optimization problem in (29) is convex in $\mathbf{P}$.

Proof: Since $\mathbf{X}(\mathbf{P})$ is affine in $\mathbf{P}$, as seen in (29a), it follows from Definition 3 that $J(\mathbf{X}(\mathbf{P}))$ is convex in $\mathbf{P}$

if $J(\mathbf{X})$ is convex in $\mathbf{X}$. Thus reducing the convexity analysis to $J(\mathbf{X})$ as expressed in (16).

The cost function $J(\mathbf{X})$ can be expressed as the sum of individual cost functions $G_n(\mathbf{Z}_n(\mathbf{X}))$ as shown in (22). Since convexity is preserved under a positive weighted sum, [31], it follows that the overall sum $J(\mathbf{X})$ is convex in $\mathbf{X}$, if the summands $G_n(\mathbf{Z}_n(\mathbf{X}))$ are convex in $\mathbf{X}$. Furthermore, given that $\mathbf{Z}_n(\mathbf{X})$ is affine in $\mathbf{X}$, as seen in (22a), the analysis is reduced to show if an arbitrary summand $G_n(\mathbf{Z}_n)$ is convex in $\mathbf{Z}_n$. For $n = k$, this is equivalent to showing if $G_k(\mathbf{Z}_k)$, as given in (21), is convex in $\mathbf{Z}_k$. □

Definition 4: Given a function $f \in C^2$, the function is convex if and only if its domain $\mathbf{dom}\, f$ is convex and its Hessian is positive semidefinite, $\nabla^2 f(x) \succeq 0, \forall x \in \mathbf{dom}\, f$, [31].

Definition 5: Given a symmetric matrix $\mathbf{A} \in \mathbb{R}^{n\times n}$, it is called positive semidefinite *if $\mathbf{x}^\mathsf{T}\mathbf{A}\mathbf{x} \geq 0, \forall x \neq 0$. Thus even its minimum eigenvalue is not negative, $\lambda_{min}(\mathbf{A}) \geq 0$, [31].*

Proposition 5: The squared error cost function $G_k(\mathbf{Z}_k)$ in (21) is not convex in $\mathbf{Z}_k$.

Proof: In order to test for convexity via the second-order convexity condition from Definition 4, first the Hessian of $G_k(\mathbf{Z}_k)$ is calculated as

$$\begin{aligned}\nabla^2 G_k(\mathbf{Z}_k) = {} & 2\begin{bmatrix}(1+\mu)^2\mathbf{I}_{2\times2} & -(1+\mu)\mathbf{R}_\phi^\mathsf{T}\\ -(1+\mu)\mathbf{R}_\phi & \mathbf{I}_{2\times2}\end{bmatrix}\\ & + 4\alpha\mathbf{L}_0\mathbf{Z}_k\left(\mathbf{Z}_k^\mathsf{T}\begin{bmatrix}2(1+\mu)\mathbf{I}_{2\times2} & -\mathbf{R}_\phi^\mathsf{T}\\ -\mathbf{R}_\phi & \mathbf{0}_{2\times2}\end{bmatrix}\right)\\ & + 2\alpha\left(\mathbf{Z}_k^\mathsf{T}\begin{bmatrix}2(1+\mu)\mathbf{I}_{2\times2} & -\mathbf{R}_\phi^\mathsf{T}\\ -\mathbf{R}_\phi & \mathbf{0}_{2\times2}\end{bmatrix}\mathbf{Z}_k\right)\mathbf{L}_0\\ & + 4\alpha\begin{bmatrix}2(1+\mu)\mathbf{I}_{2\times2} & -\mathbf{R}_\phi^\mathsf{T}\\ -\mathbf{R}_\phi & \mathbf{0}_{2\times2}\end{bmatrix}\mathbf{Z}_k\left(\mathbf{Z}_k^\mathsf{T}\mathbf{L}_0\right)\\ & + 2\alpha\left(\mathbf{Z}_k^\mathsf{T}\mathbf{L}_0\mathbf{Z}_k\right)\begin{bmatrix}2(1+\mu)\mathbf{I}_{2\times2} & -\mathbf{R}_\phi^\mathsf{T}\\ -\mathbf{R}_\phi & \mathbf{0}_{2\times2}\end{bmatrix}\\ & + 24\alpha^2\left(\mathbf{Z}_k^\mathsf{T}\mathbf{L}_0\mathbf{Z}_k\right)\mathbf{L}_0\mathbf{Z}_k\left(\mathbf{Z}_k^\mathsf{T}\mathbf{L}_0\right)\\ & + 6\alpha^2\left(\mathbf{Z}_k^\mathsf{T}\mathbf{L}_0\mathbf{Z}_k\mathbf{Z}_k^\mathsf{T}\mathbf{L}_0\mathbf{Z}_k\right)\mathbf{L}_0. \end{aligned} \tag{31}$$

According to Definition 5, if there exists a $\mathbf{Z}_k^\star$ such that $\lambda_{min}\left(\nabla^2 G_k\left(\mathbf{Z}_k^\star\right)\right) < 0$, then $\nabla^2 G_k\left(\mathbf{X}_k^\star\right)$ is not positive semidefinite, and thus $G_k(\mathbf{Z}_k)$ is not convex in $\mathbf{Z}_k$.

Given the same parameters as in the examples in Section II, $\mu = 0.05$, $\alpha = -0.05$, $\tau = 0.2\,\text{ms}$, and $\phi = 2\pi 50\tau$. Let $\mathbf{Z}_k^\star = \begin{bmatrix}2 & -2 & -4 & 4\end{bmatrix}^\mathsf{T}$, then

$$\nabla^2 G_k\left(\mathbf{Z}_k^\star\right) = \begin{bmatrix}-8.1574 & 4.8017 & -0.4488 & -0.8298\\ 4.8017 & -8.5593 & -0.7670 & -0.5492\\ -0.4488 & -0.7670 & 2 & 0\\ -0.8298 & -0.5492 & 0 & 2\end{bmatrix}, \tag{32}$$

rounded to 4 digits after the decimal point. The calculated Hessian has a negative eigenvalue of $\lambda_{min} = -13.1702$ and a relatively low condition number $\kappa = 6.5656$. Thus by counterexample $G_k(\mathbf{Z}_k)$ is not convex in $\mathbf{Z}_k$. □

Remark 1: Even though Proposition 5 states that $G_k(\mathbf{Z}_k)$ is not convex in $\mathbf{Z}_k$, and thus Theorem 2 can no longer be used to show that $J(\mathbf{X}(\mathbf{P}))$ is convex in $\mathbf{P}$, its inverse is not true, since it is a sufficient but not necessary condition. Therefore, $J(\mathbf{X}(\mathbf{P}))$ can still be convex in $\mathbf{P}$.

B. CONVEXITY REDUCED TO A LINE

This approach derives from a fundamental property of convex functions defined as follows.

Definition 6: Given a function $f : \mathbb{R}^n \mapsto \mathbb{R}$, such function is called convex *if $\mathbf{dom}\, f$ is a convex set and if for all $\mathbf{x}_1, \mathbf{x}_2 \in \mathbf{dom}\, f$, and θ with $0 \leq \theta \leq 1$, it follows that*

$$0 \leq \theta f(\mathbf{x}_1) + (1-\theta) f(\mathbf{x}_2) - f(\theta\mathbf{x}_1 + (1-\theta)\mathbf{x}_2), \tag{33}$$

which is known as Jensen's inequality, [31].

Proposition 6: For a function f, a cost function H can be defined as

$$\begin{aligned} H(\mathbf{E}) = {} & \mathbf{M}_\theta\mathbf{E} f\left(\mathbf{M}_{\mathbf{x}_1}\mathbf{E}\right) + (1-\theta) f\left(\mathbf{M}_{\mathbf{x}_2}\mathbf{E}\right)\\ & - f\left(\mathbf{M}_\theta\mathbf{E}\mathbf{M}_{\mathbf{x}_1}\mathbf{E} + (1-\mathbf{M}_\theta\mathbf{E})\mathbf{M}_{\mathbf{x}_2}\mathbf{E}\right), \end{aligned} \tag{34}$$

where

$$\mathbf{E} = \begin{bmatrix}\theta & \mathbf{x}_1^\mathsf{T} & \mathbf{x}_2^\mathsf{T}\end{bmatrix}^\mathsf{T} \tag{34a}$$

$$\theta = \mathbf{M}_\theta\mathbf{E}, \tag{34b}$$

$$\mathbf{x}_1 = \mathbf{M}_{\mathbf{x}_1}\mathbf{E}, \tag{34c}$$

$$\mathbf{x}_2 = \mathbf{M}_{\mathbf{x}_2}\mathbf{E}, \tag{34d}$$

for $\mathbf{x}_1, \mathbf{x}_2 \in \mathbf{dom}\, f$, and θ with $0 \leq \theta \leq 1$, such that the solution of the optimization problem

$$\min_{\mathbf{E}} H(\mathbf{E}), \tag{35}$$

must not be negative $H(\mathbf{E}^\star) \geq 0$ to ensure that f is convex.

Proof: The cost function in (34) is equivalent to the right-hand side of Jensen's inequality in (33). Therefore, a negative optimal cost $H(\mathbf{E}^\star) < 0$ will lead to an infringement of the inequality, thus showing that f is not convex. □

The optimization problem in (35) reduces the convexity analysis to two points in a line, as defined by the parameters of Jensen's inequality in (33). This approach can be used to find a numerical counterexample that shows if the cost function $J(\mathbf{X}(\mathbf{P}))$ of the optimization problem in (29) is not convex in $\mathbf{P}$. Since $J(\mathbf{X}(\mathbf{P}))$ includes constraints that require a system to be defined as in (23a), a numerical test was carried out for the application example system in Section V-E.

V. APPLICATION EXAMPLE

The electrical power system is transitioning from a demand-driven system to a generation-driven system due to the increasing share of renewable energy sources. These sources, mainly wind and photovoltaic systems, are connected to the power grid via power converters. One of the challenges this new technology poses is the introduction of harmonic distortion into the grid due to the switching power electronic devices involved [32]. To cope with this, a APF can be used to compensate for undesired frequencies, where the control of the reference compensation current is key, [2]. The standard control techniques (ISC, IRP, and SRF) among

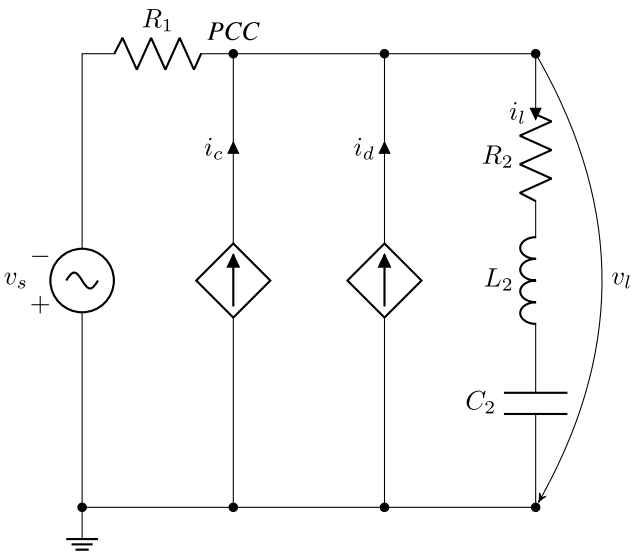

FIGURE 4. Microgrid circuit diagram.

TABLE 1. Microgrid circuit parameters.

Component	Variable	Value
Feeder line resistance	R_1	$100\,\Omega$
Load resistance	R_2	$10\,\Omega$
Load inductance	L_2	$100\,\text{mH}$
Load capacitance	C_2	$10\,\text{mF}$

more advanced approaches to operate a APF were already introduced in Section I. The following application example will illustrate how the proposed LCMPC controller can be used to operate a APF for harmonic compensation.

A. ELECTRIC GRID CIRCUIT MODEL

To illustrate the potential of the controller, a simple microgrid is defined as shown in Fig. 4. The system is designed for a fundamental frequency of $f = 50\,\text{Hz}$ with a $400\,\text{V}$ connection to an external distribution grid, represented by the ideal supply voltage v_s. Parallel to it is the APF line for the controller compensation input, represented by the ideal controlled current source i_c. Next to it is the controlled ideal current source i_d that introduces the harmonic distortion to the point of common coupling (PCC). Finally, on the right side as the compensation target is the system series RLC load with current i_l and voltage v_l. Table 1 shows the parameters of the system.

The simplification of i_c and i_d as ideal controlled current sources is done to achieve a linear model of the system since the focus of the application example is on the controller performance rather than model complexity. Therefore, a continuous-time state-space model of the system can be formulated as

$$\dot{\mathbf{x}}(t) = \mathbf{A}_c\mathbf{x}(t) + \mathbf{b}_c u(t) + \mathbf{F}_c\mathbf{v}(t), \tag{36a}$$
$$\mathbf{y}_k = \mathbf{C}_c\mathbf{x}(t), \tag{36b}$$

with state vector $\mathbf{x} = \begin{bmatrix} q_l & i_l \end{bmatrix}^\mathsf{T}$, where q_l is the charge of the load current i_l; input $u = i_c$; measured input disturbance vector $\mathbf{v} = \begin{bmatrix} i_d & v_s \end{bmatrix}^\mathsf{T}$; and output vector $\mathbf{y} = \begin{bmatrix} v_c & i_l \end{bmatrix}^\mathsf{T}$, where v_c is the voltage of the capacitor C_2. The parameters of the model are

$$\mathbf{A}_c = \begin{bmatrix} 0 & 1 \\ -\dfrac{1}{C_2 L_2} & -\dfrac{R_2 + R_1}{L_2} \end{bmatrix}, \tag{36c}$$
$$\mathbf{b}_c = \begin{bmatrix} 0 & \dfrac{R_1}{L_2} \end{bmatrix}^\mathsf{T}, \tag{36d}$$
$$\mathbf{F}_c = \begin{bmatrix} 0 & 0 \\ \dfrac{R_1}{L_2} & \dfrac{1}{L_2} \end{bmatrix}, \tag{36e}$$
$$\mathbf{C}_c = \begin{bmatrix} \dfrac{1}{C_2} & 0 \\ 0 & 1 \end{bmatrix}. \tag{36f}$$

B. NORMAL FORM SYSTEM TRANSFORMATION

As stated in Definition 1, the supercritical Neimark-Sacker bifurcation normal form will drive the state dynamics to a circular shape of radius ρ as defined in (8). This means that each state will have a fundamental harmonic shape over time.

This particular configuration is the key to use the LCMPC for harmonic compensation. However, to implement it, both states in the target system must tend towards the same amplitude, ρ. This is not necessarily the desired outcome in the application example system of (36), where q_l and i_l could have different target amplitudes. Therefore, a system transformation to scale both states in (36) to have the same amplitude, in this case for simplicity $\rho = 1$, is performed as

$$\tilde{\mathbf{x}} = \mathbf{T}^{-1}\mathbf{x}, \tag{37}$$

where

$$\mathbf{T} = \begin{bmatrix} 0 & \rho_v C_2 \\ \rho_i & 0 \end{bmatrix}, \tag{37a}$$

and ρ_v and ρ_i are the desired steady-state undisturbed amplitudes of v_c and i_l respectively. This transformation applies to all the state-space parameters of (36), leading to

$$\tilde{\mathbf{A}} = \mathbf{T}^{-1}\mathbf{A}_c\mathbf{T}, \tag{37b}$$
$$\begin{bmatrix} \tilde{\mathbf{b}} & \tilde{\mathbf{F}} \end{bmatrix} = \mathbf{T}^{-1}\begin{bmatrix} \mathbf{b}_c & \mathbf{F}_c \end{bmatrix}, \tag{37c}$$
$$\tilde{\mathbf{C}} = \mathbf{C}_c\mathbf{T}. \tag{37d}$$

Finally, since the LCMPC requires a discrete-time model, the transformed state-space model is taken to discrete-time using the zero-order-hold method for a given sampling time τ; leading to the final state-space parameters: $\mathbf{A}$, $\mathbf{b}$, $\mathbf{F}$, and $\mathbf{C}$.

C. SIMULATION SETUP

The study simulated 10 s of grid operation, which amounts to 500 fundamental periods at a sampling time of $\tau = 200\,\mu\text{s}$.

For the controller, the prediction horizon was set to two fundamental periods as $H_p = 200$, and the limit cycle parameters were: $\mu = 10^{-1}$, $\alpha = -10^{-1}$, and $\phi = 2\pi f \tau$. Regarding the input disturbance current, the study was split into two disturbance scenarios: A and B. For scenario A, the uncontrollable measured input disturbance current was defined as follows

$$i_{d\mathrm{A}}(t) = 2\sin\left(3\omega t + \arctan\left(\frac{4}{3}\right)\right) + 3\sin\left(5\omega t + \arctan\left(\frac{3}{4}\right) + \frac{\pi}{2}\right), \quad (38)$$

to reflect the typical harmonic content found in nonlinear loads such as rectifiers, while the harmonic upper band for the input was set to $h_{\mathrm{A}} = 5$ to tighten the search space. For scenario B, the uncontrollable measured input disturbance current was defined as follows

$$\begin{aligned} i_{d\mathrm{B}}(t) = {} & 2\sin\left(3\omega t + \arctan\left(\frac{4}{3}\right)\right) \\ & + 3\sin\left(5\omega t + \arctan\left(\frac{3}{4}\right) + \frac{\pi}{2}\right) \\ & + 2\sin\left(7\omega t + \arctan\left(\sqrt{3}\right)\right) \\ & + 3\sin\left(9\omega t + \arctan\left(\frac{1}{\sqrt{3}}\right) + \frac{\pi}{2}\right), \end{aligned} \quad (39)$$

with the harmonic upper band for the input set to $h_{\mathrm{B}} = 10$ and phase shift of $\frac{3\pi}{10}$ to the supply voltage v_s. The idea is to show the scalability of the approach when including more harmonics and the effect of different initial phase conditions.

For the LCMPC control closed loop, complete knowledge of the system states was assumed $\hat{\mathbf{x}} = \mathbf{x}$ (no observer required); thus, access to the normalized initial values $\tilde{\mathbf{x}}_0$, which are also used to define the initial amplitude and phase, is considered. In the case of the predictor, a moving window delay of one fundamental period was considered, meaning that $\hat{\mathbf{v}}$ is assumed to be the same as the last period measured $\mathbf{v}$, leveraging the expected periodic behavior of the system. For the feedback policy, a periodic receding horizon strategy was used to reduce computational time, as introduced in [33]. In this hybrid regime, the optimal input sequence $\mathbf{U}^\star$ is computed once per fundamental period, during which it will be given to the plant in a feed-forward manner until the new $\mathbf{U}^\star$ is calculated once the feedback measurements are updated in the next period. This strategy is viable since only steady-state periodic disturbances are assumed.

The optimization solver used was `fminunc` from MATLAB®, designed for general unconstrained minimization. For this setup, the equality constraints of (29) were embedded into the cost function; if there would be inequality constraints, e.g. physical limitations of the actuator, a different solver would be needed. As optimization algorithm, `trust-region` was selected with the default optimality and step tolerances of 10^{-6}. This algorithm also allows for the use of an analytical formulation of the gradient and Hessian to further accelerate computation. These were calculated as explained in Appendix B.

The simulations were carried out in an Intel®Core™ i7-9850H CPU @ 2.60 GHz with 16 GB of RAM, with operating system Microsoft® Windows® 10 Enterprise x64 Edition version 10.0 build 19041, running MATLAB® version 9.9 R2020b, with the Global Optimization Toolbox version 4.4.

D. SIMULATION RESULTS

The total computation time of scenario A was 26.44 s, with an average of 52.88 ms per fundamental period, while scenario B took only 19.59 s, with an average of 39.18 ms per fundamental period. This shows that the controller does not have scalability issues since the changes in initial conditions seem to have a bigger impact than the number of harmonics considered. Additionally, the average time per period of both scenarios is within the order of magnitude of the 20 ms computation window of a fundamental period at 50 Hz, which is critical as the controller is further developed towards a real-time operation setup. In Fig. 5, the simulation results for scenario A of the first two periods (left column) and the last two periods (right column) are shown, while for scenario B, these are shown in Fig 6. From top to bottom, the rows of signals presented are the outputs, the capacitor voltage v_c and load current i_l, and the controlled input compensation current i_c. The red dashed signals denote the disturbed uncompensated response, the green dotted signals denote the undisturbed ($i_d = 0$) uncompensated response, and the solid blue lines denote the disturbed controlled response. It can be seen that for both scenarios, both output signals achieve a fundamental harmonic shape when controlled; however, there is a slight phase shift when compared to the undisturbed signals in the first periods, especially in scenario A. This phase shift can be associated with the initial conditions since they dictate the initial phase and are affected by the harmonic disturbance. This effect can be attenuated over time, as seen in the last two periods where the phase shift is almost gone in scenario A.

To properly analyze the quality of the compensation, Fig. 7 shows the root mean square (RMS) and the total harmonic distortion (THD) values of the output signals over time in a moving window of one fundamental period for scenario A, while Fig. 8 shows the outcome for scenario B. Since the dynamic response of scenario B is considerably faster, Fig. Fig. 8 includes zoom boxes for the first three periods following the first measurement period to capture these dynamics. In the case of the RMS in the upper plots of the figures, the output calculations for both scenarios, denoted by the solid blue signals, are tending towards their undisturbed steady-state values asymptotically, $\rho_v = 7.88 \times 10^{-1}$ V for v_c and $\rho_i = 2.47$ A for i_l, which are denoted by the green dotted lines. For the THD calculations in the lower plots of the figure, the controller manages to compensate the harmonic distortion in the output, denoted by the solid blue signals, from the initial disturbed

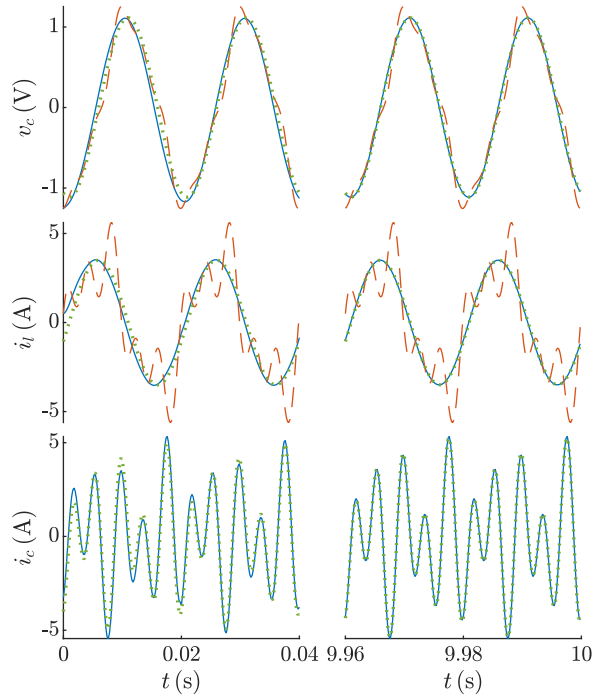

FIGURE 5. Scenario A simulation results for the capacitor voltage v_c, load current i_l, and compensation current i_c.

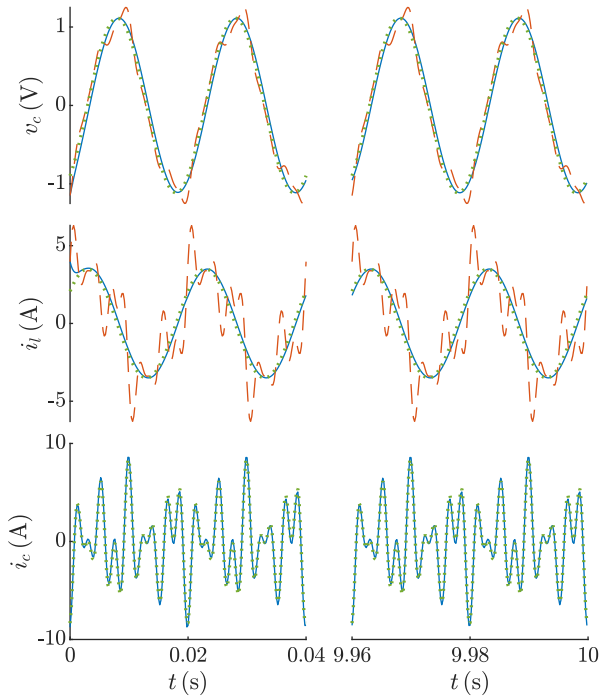

FIGURE 6. Scenario B simulation results for the capacitor voltage v_c, load current i_l, and compensation current i_c.

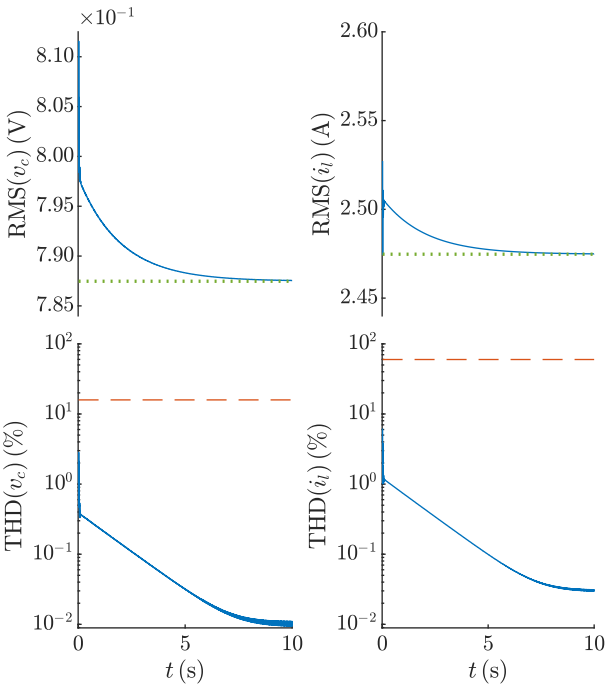

FIGURE 7. Scenario A RMS and THD results for the capacitor voltage v_c and load current i_l.

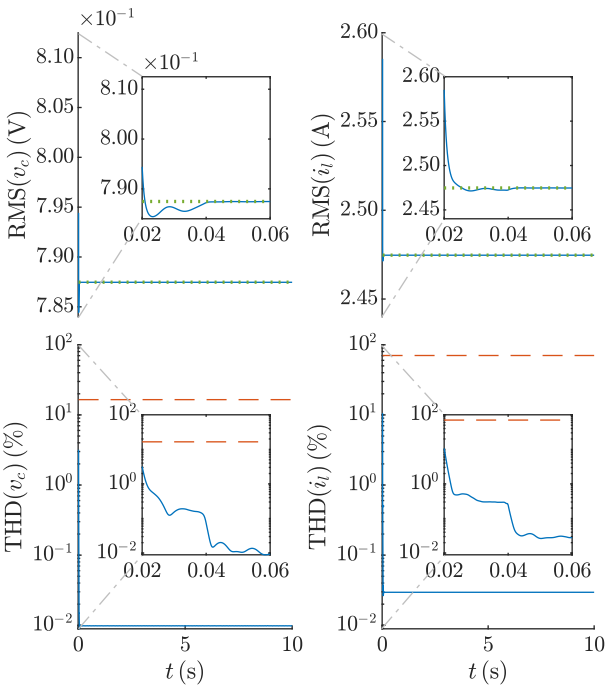

FIGURE 8. Scenario B RMS and THD results for the capacitor voltage v_c and load current i_l.

uncompensated values of 15.9% for v_c and 59.8% for i_l, denoted by the red dashed lines, down to 1.01×10^{-2}% for v_c and 2.99×10^{-2}% for i_l by the end of the simulation for scenario A, while for scenario B it goes from 16.5% to 0.98×10^{-2}% for v_c and from 70.3% to 2.95×10^{-2}% for i_l. These results are considerably below the reference limit value of 8% THD for voltages defined in the European Norm: EN 50160, [34]. In both analyses, scenario B has considerably faster dynamics than scenario A, as the compensation is achieved almost immediately. This can be mainly attributed to the change in phase for the initial conditions, as will be seen in the following figures.

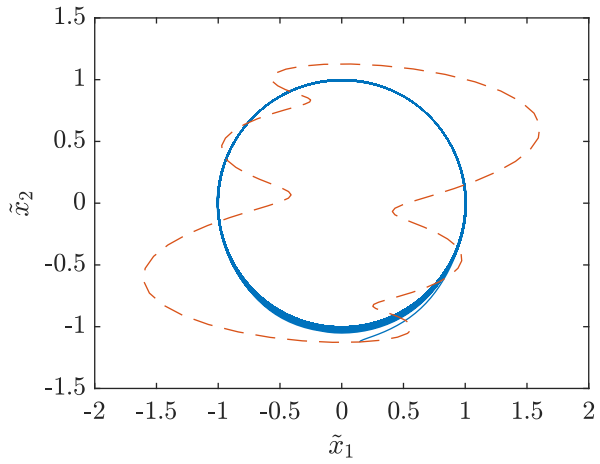

FIGURE 9. Scenario A normal form transformation states phase space.

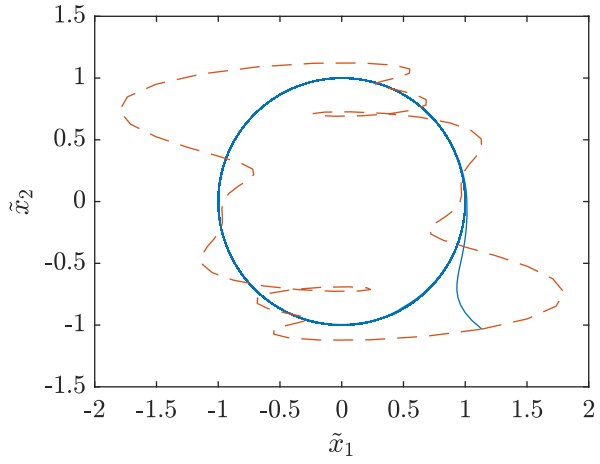

FIGURE 10. Scenario B normal form transformation states phase space.

When looking at the results from the phase-space system transformation of the normal form, as portrayed in Fig. 9 for scenario A and in Fig. 10 for scenario B, the limit cycle dynamics of the controller become evident. In the phase plots, the red dashed signals denote the uncompensated disturbed states, while the solid blue signals denote the compensated disturbed states. It can be observed how the controlled states orbit towards the circular limit cycle of radius one at the origin. This behavior is in agreement with the design parameters of the controller that lead to the supercritical Neimark-Sacker bifurcation normal form, as described in Definition 1. Comparing both scenarios, the faster dynamics of scenario B become evident, as the disturbed states converge much faster. Recalling Fig. 1, this behavior is expected since the further away from the limit cycle, the more aggressive the attraction effect is, as shown by the vector field denoted by the red arrows.

E. CONVEXITY NUMERICAL TEST

As introduced in Section IV-B, the optimization problem in (35) was set up for the cost function $J(\mathbf{X}(\mathbf{P}))$ from (29), subject to the constraints of the system described in Section V-A. A set of results for the optimization problem $H^\star$ under different solver configurations from Matlab Optimization Toolbox™ is given in Table 2.

TABLE 2. Jensen's inequality minimization results.

Solver	$\theta^\star$	mean$(\|\mathbf{x}_i^\star\|)$	$\|\mathbf{x}_1^\star - \mathbf{x}_2^\star\|$	$H^\star$
Genetic Algorithm	9.99×10^{-1}	8.43	1.07×10^{-3}	-2.48×10^{-14}
Global Search	4.83×10^{-1}	3.16×10^{4}	8.36×10^{-5}	-6.29×10^{6}
Multi Start	5.34×10^{-17}	7.91×10^{4}	6.91×10^{4}	-1.34×10^{9}

TABLE 3. Jensen's inequality constrained minimization results.

Solver	$\theta^\star$	mean$(\|\mathbf{x}_i^\star\|)$	$\|\mathbf{x}_1^\star - \mathbf{x}_2^\star\|$	$H^\star$
Genetic Algorithm	9.99×10^{-1}	7.48	7.51×10^{-3}	3.65×10^{-10}
Global Search	3.94×10^{-1}	4.13	6.21×10^{-3}	4.79×10^{-7}
Multi Start	3.94×10^{-1}	4.13	6.21×10^{-3}	4.79×10^{-7}

The results show that the cost function $H^\star$ reaches negative values, thus infringing the Jensen's inequality in (33), only when either $\mathbf{x}_1^\star$ and $\mathbf{x}_2^\star$ are too close in magnitude, or $\theta^\star$ takes an extreme value from its domain $0 \leq \theta \leq 1$. Since the infringements only occur in these extreme ill-conditioned scenarios prone to numerical problems, the results are considered inconclusive. Therefore, to steer the solver search space away from these extreme solutions, an additional constraint is formulated as

$$\Delta_{\min} - \frac{\|\mathbf{x}_1 - \mathbf{x}_2\|}{\max\left(\|\mathbf{x}_1\|, \|\mathbf{x}_2\|\right)} \leq 0. \tag{40}$$

This nonlinear constraint ensures that the normalized absolute distance between $\mathbf{x}_1$ and $\mathbf{x}_2$ is not smaller than $\Delta_{\min}$. Implementing this new constraint with $\Delta_{\min} = 1 \times 10^{-3}$ and restricting θ to $[0.001, 0.999]$, leads to a new set of results given in Table 3.

This time, none of the solutions lead to a negative $H^\star$; thus, Jensen's inequality still holds. Therefore, the convexity of $J(\mathbf{X}(\mathbf{P}))$ in $\mathbf{P}$ cannot be rejected by the results of these numerical simulations for the system in Section V-A.

F. QUALITATIVE COMPARISON

Table 4 gives a qualitative comparison between the LCMPC and other common APF control approaches, which were introduced in more detail in Section I.

The classical PI controller in APF applications is equipped with an LPF making it easy to compute but slow in response time. It is typically designed for a specific load scenario; therefore, parameter variations pose accuracy problems. Overall, the disturbance rejection can be improved with more elaborate control schemes, [1]–[3].

Repetitive controllers have the advantage of a low computational burden, although the states of one period need to be stored. The calculations of the control signal are very efficient since these are mainly transfer functions. If the harmonic disturbance is not changing for several fundamental periods,

TABLE 4. Qualitative comparison of different APF control approaches.

Controller	Computation time	Disturbance rejection	Accuracy	Parameter sensitivity	Response time
PI+LPF	low	low	low	high	slow
RC	low	mid	mid	low	mid
SMC	low	high	mid	low	fast
DBMPC	low-mid	mid	high	mid	very fast
LCMPC	mid-high	mid	high	mid	fast

it can be compensated accurately. Repetitive controllers are tuned for the applications by adapting their filters; thus, only parameter variations within the specified boundaries can be addressed. Depending on the aggressiveness of the filters, there is a trade-off between the robustness of the setup versus the response time, [9]–[17].

Sliding mode controllers require a relatively low computation effort in their more simple implementations. The main appealing attributes of SMC are its fast response and robustness against disturbances and parameter variations. However, when tuned too aggressively, they can lead to chattering, which is their main drawback since it affects accuracy and stability, [20]–[22].

Deadbeat MPCs has a short prediction horizon and is thus a fast actuation type of optimal controller. This setup allows for very fast and accurate responses with relatively low computational effort when unconstrained. However, due to the short prediction horizon, preventive control actions against periodic disturbances are limited, and as with other model-based approaches, it is sensitive to unmeasurable parameter variations, [23], [24].

The LCMPC, similarly to other optimal controllers, allows for high accuracy and fast response times. The main difference is that it takes full advantage of periodic behaviors due to its limit-cycle dynamics and periodic prediction horizon, which is beneficial against measurable periodic disturbances. However, computation time is still an issue in its current state. Even though the optimal input is calculated only once per period, the online solver is still quite computationally intensive. Therefore, additional work on convex formulations is still required. As the method is developed further towards real-time implementation, quantitative comparisons are planned.

VI. CONCLUSION

The developed LCMPC approach embeds the attractor dynamics of a stable circular limit cycle directly into its cost function as a nonlinear shape residual. These dynamics enable the controller to drive a system's target states to a fundamental harmonic shape with a specific amplitude and frequency. This control action is especially beneficial in applications where a periodic behavior is desired. This is illustrated in the application example, where the LCMPC manages to effectively mitigate both harmonic disturbance scenarios while reaching the correct amplitude in the target states. This was achieved in both scenarios with minimal impact to performance and computation time; thus, showing good scalability characteristics of the controller.

When analyzing the cost function structure, convexity could not be proved by function decomposition. However, as shown by the numerical test results, convexity can still not be discarded since no well-conditioned counter-example was found. Further analysis is required to determine whether the cost function optimization is a convex problem or if it can be transformed into one, particularly when restricting the decision space to a specific system. This analysis is the key to enabling the real-time implementation of the LCMPC, e.g., a hardware-in-the-loop setup, as convex optimization problems can be solved online in conventional microcontrollers with a predictable computational time.

Regarding stability certificates, the presented radius critical points analysis opens the possibility for further research on the formulation of operating regions where local asymptotic stability could be guaranteed.

From an application perspective, ongoing research is focused on more complex approaches of disturbance prediction and initial phase estimation, and their effect on the LCMPC performance, especially in scenarios with uncertainty. Direct comparisons against standard controllers as well as other MPC approaches are also planned.

Beyond harmonic compensation, other power quality concepts are to be explored. In particular, grid forming converter control is of special interest, as the periodic dynamics of limit cycles have proven their efficacy in recent approaches, i.e., dVOC.

APPENDIX A
PERIODIC ORBITS

Periodic orbits are cycles with oscillatory behavior. For discrete-time systems, they are defined as follows.

Definition 7: A cycle Γ *is a periodic orbit if, for all* $x_0 \in \Gamma$, *it satisfies the map* $\varphi : X \mapsto X$, *given as*

$$\varphi_{k+T} x_0 = \varphi_k x_0, \tag{41}$$

where $\varphi_k x_0 = x_k$ *for discrete time* $k \in \mathbb{Z}$ *and* $T \in \mathbb{Z}_{>0}$, *[29].*

The minimal T, which satisfies the properties in Definition 7, is called the period of the cycle Γ, [29]. This means that if a system starts at x_0, after exactly T iterations of the map, it will return to x_0, hence the oscillatory behavior.

For starting points outside the orbit, there is a special case given as follows.

Definition 8: A periodic orbit Γ_0 *is called a limit cycle if there exists a point in its neighborhood that is not in the orbit, such that its limit set is exactly* Γ_0, *as time moves forward (*ω*-limit set) or backward (*α*-limit set), [35].*

APPENDIX B
GRADIENT AND HESSIAN

Many algorithms for solving optimization problems, such as the gradient descent method, greatly benefit from having access to an analytical gradient and Hessian of the cost

function, [31]. This is possible for the proposed cost function in (16) since it is a twice-differentiable function. The following gradient and Hessian derivations have been done using the symbolic matrix calculus tool from [36], [37].

The gradient of (16) is given as

$$\begin{aligned}\frac{\partial J}{\partial \mathbf{X}} &= 2\mathbf{Q}_2\mathbf{X} + 2\alpha\mathbf{Q}_4\left((\mathbf{L}\,(\mathbf{X}\circ\mathbf{X}))\circ\mathbf{X}\right)\\ &\quad + 4\alpha\left(\mathbf{L}\left(\left(\mathbf{Q}_4^{\mathsf{T}}\mathbf{X}\right)\circ\mathbf{X}\right)\right)\circ\mathbf{X} + 2\alpha\left(\mathbf{Q}_4^{\mathsf{T}}\mathbf{X}\right)\circ(\mathbf{L}\,(\mathbf{X}\circ\mathbf{X}))\\ &\quad + 4\alpha^2\left(\mathbf{L}\left((\mathbf{L}\,(\mathbf{X}\circ\mathbf{X}))\circ(\mathbf{X}\circ\mathbf{X})\right)\right)\circ\mathbf{X}\\ &\quad + 2\alpha^2\left(\mathbf{L}\,(\mathbf{X}\circ\mathbf{X})\right)\circ\mathbf{X}\circ(\mathbf{L}\,(\mathbf{X}\circ\mathbf{X}))\,. \end{aligned} \tag{42}$$

While the Hessian is

$$\begin{aligned}\frac{\partial^2 J}{\partial \mathbf{X}_i\mathbf{X}_j} &= 2\mathbf{Q}_2 + 4\alpha\mathbf{Q}_4\,\mathrm{diag}\,(\mathbf{X})\,\mathbf{L}\,\mathrm{diag}\,(\mathbf{X})\\ &\quad + 2\alpha\mathbf{Q}_4\,\mathrm{diag}\left((\mathbf{X}\circ\mathbf{X})^{\mathsf{T}}\mathbf{L}\right) + 4\alpha\,\mathrm{diag}\,(\mathbf{X})\,\mathbf{L}\,\mathrm{diag}\,(\mathbf{X})\,\mathbf{Q}_4^{\mathsf{T}}\\ &\quad + 4\alpha\,\mathrm{diag}\,(\mathbf{X})\,\mathbf{L}\,\mathrm{diag}\left(\mathbf{X}^{\mathsf{T}}\mathbf{Q}_4\right)\\ &\quad + 4\alpha\,\mathrm{diag}\left(\mathbf{L}\left(\left(\mathbf{Q}_4^{\mathsf{T}}\mathbf{X}\right)\circ\mathbf{X}\right)\right)\\ &\quad + 2\alpha\,\mathrm{diag}\,(\mathbf{L}\,(\mathbf{X}\circ\mathbf{X}))\,\mathbf{Q}_4^{\mathsf{T}} + 4\alpha\,\mathrm{diag}\left(\mathbf{Q}_4^{\mathsf{T}}\mathbf{X}\right)\mathbf{L}\,\mathrm{diag}\,(\mathbf{X})\\ &\quad + 8\alpha^2\,\mathrm{diag}\,(\mathbf{X})\,\mathbf{L}\,\mathrm{diag}\,(\mathbf{X}\circ\mathbf{X})\,\mathbf{L}\,\mathrm{diag}\,(\mathbf{X})\\ &\quad + 8\alpha^2\,\mathrm{diag}\,(\mathbf{X})\,\mathbf{L}\,\mathrm{diag}\,((\mathbf{L}\,(\mathbf{X}\circ\mathbf{X}))\circ\mathbf{X})\\ &\quad + 4\alpha^2\,\mathrm{diag}\,(\mathbf{L}\,((\mathbf{L}\,(\mathbf{X}\circ\mathbf{X}))\circ\mathbf{X}\circ\mathbf{X}))\\ &\quad + 8\alpha^2\,\mathrm{diag}\,((\mathbf{L}\,(\mathbf{X}\circ\mathbf{X}))\circ\mathbf{X})\,\mathbf{L}\,\mathrm{diag}\,(\mathbf{X})\\ &\quad + 2\alpha^2\,\mathrm{diag}\,((\mathbf{L}\,(\mathbf{X}\circ\mathbf{X}))\circ(\mathbf{L}\,(\mathbf{X}\circ\mathbf{X})))\,, \end{aligned} \tag{43}$$

where the $\mathrm{diag}\,(v)$ operator gives a square diagonal matrix with the vector v as its main diagonal.

The gradient can be calculated in terms of the Fourier approximation of $\mathbf{X}\,(\mathbf{P})$, as expressed in the lifted system in (29a), applying the chain rule to (42), so that

$$\frac{\partial J\,(\mathbf{X}\,(\mathbf{P}))}{\partial \mathbf{P}} = \frac{\partial J}{\partial \mathbf{X}}\frac{\partial \mathbf{X}}{\partial \mathbf{P}} = \left(\mathbf{M}^{\mathsf{T}}\otimes\mathbf{I}_{m\times m}\right)\Theta^{\mathsf{T}}\frac{\partial J}{\partial \mathbf{X}}. \tag{44}$$

Similarly, the Hessian can be calculated in terms of the Fourier approximation by applying the second-order chain rule (Faà di Bruno's formula) to (43), which leads to

$$\begin{aligned}\frac{\partial^2 J\,(\mathbf{X}\,(\mathbf{P}))}{\partial \mathbf{P}_i\mathbf{P}_j} &= \frac{\partial^2 J}{\partial \mathbf{X}_i\mathbf{X}_j}\left(\frac{\partial \mathbf{X}}{\partial \mathbf{P}}\right)^2 + \frac{\partial J}{\partial \mathbf{X}}\frac{\partial^2 \mathbf{X}}{\partial \mathbf{P}_i\mathbf{P}_j}\\ &= \left(\mathbf{M}^{\mathsf{T}}\otimes\mathbf{I}_{m\times m}\right)\Theta^{\mathsf{T}}\frac{\partial^2 J}{\partial \mathbf{X}_i\mathbf{X}_j}\Theta\left(\mathbf{M}\otimes\mathbf{I}_{m\times m}\right). \end{aligned} \tag{45}$$

REFERENCES

[1] H. Akagi, "Active harmonic filters," *Proc. IEEE*, vol. 93, no. 12, pp. 2128–2141, Dec. 2005.

[2] P. Kumar and M. K. Mishra, "A comparative study of control theories for realizing APFs in distribution power systems," in *Proc. Nat. Power Syst. Conf. (NPSC)*, Dec. 2016, pp. 1–6.

[3] Y. Hoon, M. M. Radzi, M. Hassan, and N. Mailah, "Control algorithms of shunt active power filter for harmonics mitigation: A review," *Energies*, vol. 10, no. 12, p. 2038, Dec. 2017.

[4] Q.-N. Trinh and H.-H. Lee, "An advanced current control strategy for three-phase shunt active power filters," *IEEE Trans. Ind. Electron.*, vol. 60, no. 12, pp. 5400–5410, Dec. 2013.

[5] H. Patel and V. Agarwal, "Control of a stand-alone inverter-based distributed generation source for voltage regulation and harmonic compensation," *IEEE Trans. Power Del.*, vol. 23, no. 2, pp. 1113–1120, Apr. 2008.

[6] A. M. dos Santos Alonso, D. I. Brandao, T. Caldognetto, F. P. Marafão, and P. Mattavelli, "A selective harmonic compensation and power control approach exploiting distributed electronic converters in microgrids," *Int. J. Electr. Power Energy Syst.*, vol. 115, Feb. 2020, Art. no. 105452.

[7] A. Kalair, N. Abas, A. R. Kalair, Z. Saleem, and N. Khan, "Review of harmonic analysis, modeling and mitigation techniques," *Renew. Sustain. Energy Rev.*, vol. 78, pp. 1152–1187, Oct. 2017.

[8] T. Inoue, M. Nakano, T. Kubo, S. Matsumoto, and H. Baba, "High accuracy control of a proton synchrotron magnet power supply," *IFAC Proc. Volumes*, vol. 14, no. 2, pp. 3137–3142, Aug. 1981.

[9] P. Mattavelli and F. P. Marafao, "Repetitive-based control for selective harmonic compensation in active power filters," *IEEE Trans. Ind. Electron.*, vol. 51, no. 5, pp. 1018–1024, Oct. 2004.

[10] G. Escobar, P. R. Martinez, J. Leyva-Ramos, and P. Mattavelli, "A negative feedback repetitive control scheme for harmonic compensation," *IEEE Trans. Ind. Electron.*, vol. 53, no. 4, pp. 1383–1386, Jun. 2006.

[11] A. Garcia-Cerrada, O. Pinzon-Ardila, V. Feliu-Batlle, P. Roncero-Sanchez, and P. Garcia-Gonzalez, "Application of a repetitive controller for a three-phase active power filter," *IEEE Trans. Power Electron.*, vol. 22, no. 1, pp. 237–246, Jan. 2007.

[12] R. Grino, R. Cardoner, R. Costa-Castello, and E. Fossas, "Digital repetitive control of a three-phase four-wire shunt active filter," *IEEE Trans. Ind. Electron.*, vol. 54, no. 3, pp. 1495–1503, Jun. 2007.

[13] G. Pandove and M. Singh, "Robust repetitive control design for a three-phase four wire shunt active power filter," *IEEE Trans. Ind. Informat.*, vol. 15, no. 5, pp. 2810–2818, May 2019.

[14] G. A. Ramos and R. Costa-Castelló, "Power factor correction and harmonic compensation using second-order odd-harmonic repetitive control," *IET Control Theory Appl.*, vol. 6, no. 11, pp. 1633–1644, Jul. 2012.

[15] Z.-X. Zou, K. Zhou, Z. Wang, and M. Cheng, "Frequency-adaptive fractional-order repetitive control of shunt active power filters," *IEEE Trans. Ind. Electron.*, vol. 62, no. 3, pp. 1659–1668, Mar. 2015.

[16] H. Geng, Z. Zheng, T. Zou, B. Chu, and A. Chandra, "Fast repetitive control with harmonic correction loops for shunt active power filter applied in weak grid," *IEEE Trans. Ind. Appl.*, vol. 55, no. 3, pp. 3198–3206, May 2019.

[17] C. Xie, X. Zhao, M. Savaghebi, L. Meng, J. M. Guerrero, and J. C. Vasquez, "Multirate fractional-order repetitive control of shunt active power filter suitable for microgrid applications," *IEEE J. Emerg. Sel. Topics Power Electron.*, vol. 5, no. 2, pp. 809–819, Jun. 2017.

[18] S. V. Emelyanov, *Variable Structure Control Systems*. Moscow, Russia: Nauka, 1967.

[19] V. I. Utkin, *Sliding Modes and their Application to Variable Structure Systems* (Theoretical Foundations of Engineering Cybernetics). Moscow, Russia: Nauka, 1974.

[20] P. F. Wojciak and D. A. Torrey, "The design and implementation of active power filters based on variable structure system concepts," in *Proc. Conf. Rec. IEEE Ind. Appl. Soc. Annu. Meeting*, vol. 1, Oct. 1992, pp. 850–857.

[21] S. Kang and K. Kim, "Sliding mode harmonic compensation strategy for power quality improvement of a grid-connected inverter under distorted grid condition," *IET Power Electron.*, vol. 8, no. 8, pp. 1461–1472, Aug. 2015.

[22] J. Fei, N. Liu, S. Hou, and Y. Fang, "Neural network complementary sliding mode current control of active power filter," *IEEE Access*, vol. 9, pp. 25681–25690, 2021.

[23] A. Timbus, M. Liserre, R. Teodorescu, P. Rodriguez, and F. Blaabjerg, "Evaluation of current controllers for distributed power generation systems," *IEEE Trans. Power Electron.*, vol. 24, no. 3, pp. 654–664, Mar. 2009.

[24] J. R. Fischer, S. A. González, I. Carugati, M. A. Herrán, M. G. Judewicz, and D. O. Carrica, "Robust predictive control of grid-tied converters based on direct power control," *IEEE Trans. Power Electron.*, vol. 29, no. 10, pp. 5634–5643, Oct. 2014.

[25] J.-H. Hours, M. N. Zeilinger, R. Gondhalekar, and C. N. Jones, "Constrained spectrum control," *IEEE Trans. Autom. Control*, vol. 60, no. 7, pp. 1969–1974, Jul. 2015.

[26] M. Colombino, D. Groß, J.-S. Brouillon, and F. Dörfler, "Global phase and magnitude synchronization of coupled oscillators with application to the control of grid-forming power inverters," *IEEE Trans. Autom. Control*, vol. 64, no. 11, pp. 4496–4511, Nov. 2019.
[27] C. C. Yáñez, G. Lichtenberg, G. Pangalos, and J. S. Sáez, "An approach to state signal shaping by limit cycle model predictive control," *IFAC-PapersOnLine*, vol. 53, no. 2, pp. 6056–6061, 2020.
[28] Y. Ding and Q. Zhang, "Simplest normal forms of generalized neimark-sacker bifurcation," *Trans. Tianjin Univ.*, vol. 15, no. 4, pp. 260–265, Aug. 2009.
[29] Y. A. Kuznetsov, *Elements of Applied Bifurcation Theory* (Applied Mathematical Sciences), vol. 112, 2nd ed. I. Karatzas and M. Yor, Eds. New York, NY, USA: Springer-Verlag, 1998.
[30] J. M. Maciejowski, *Predictive Control With Constraints*. London, U.K.: Pearson, 2002.
[31] S. P. Boyd and L. Vandenberghe, *Convex Optimization*. Cambridge, U.K.: Cambridge Univ. Press, 2004.
[32] X. Liang, "Emerging power quality challenges due to integration of renewable energy sources," *IEEE Trans. Ind. Appl.*, vol. 53, no. 2, pp. 855–866, Mar. 2017.
[33] C. C. Yáñez, G. Pangalos, and G. Lichtenberg, "An approach to linear state signal shaping by quadratic model predictive control," in *Proc. Eur. Control Conf. (ECC)*. Limassol, Cyprus: IEEE, Jun. 2018, pp. 1–6.
[34] *Voltage Characteristics of Electricity Supplied By Public Electricity Networks*, Standard EN 50160:2010, Physical Characteristics of Electrical Energy, European Committee for Electrotechnical Standardization, Mar. 2020.
[35] V. G. Ivancevic and T. T. Ivancevic, *Computational Mind: A Complex Dynamics Perspective* (Studies in Computational Intelligence), vol. 60, 1st ed. Berlin, Germany: Springer-Verlag, 2007.
[36] S. Laue, M. Mitterreiter, and J. Giesen, "Computing higher order derivatives of matrix and tensor expressions," in *Proc. Adv. Neural Inf. Process. Syst. (NIPS)*, 2018, pp. 2755–2764.
[37] S. Laue, M. Mitterreiter, and J. Giesen, "A simple and efficient tensor calculus," in *Proc. AAAI Conf. Artif. Intell.*, Apr. 2020, vol. 34, no. 4, pp. 4527–4534.

CARLOS CATERIANO YÁÑEZ was born in Arequipa, Peru, in 1990. He received the B.Eng. degree in industrial and systems engineering from the University of Piura, Lima, Peru, in 2012, and the M.Eng. degree in renewable energy systems from the Hamburg University of Applied Sciences, Hamburg, Germany, in 2017. He is currently pursuing the joint Ph.D. degree in automation, robotics, and industrial computer science with Universitat Politècnica de València, Valencia, Spain, in cooperation with the Hamburg University of Applied Sciences.

Since 2017, he has been working at the Fraunhofer-Gesellschaft zur Förderung der angewandten Forschung e.V., Hamburg. His research interests include model predictive control and its applications in the field of power systems integrated with renewable energy sources.

GERWALD LICHTENBERG received the Diploma degree in physics from the University of Hamburg, in 1992, the Ph.D. degree in control engineering from the Hamburg University of Technology, in 1998, and the Habilitation degree, in 2012.

He is currently a Professor of physics and control systems at the Faculty Life Sciences, Hamburg University of Applied Sciences. His research interests include model-based and learning control as well as fault diagnosis of complex systems such as local energy networks, building systems, and particle accelerators. The methodological focus of his work is on tensor decomposition methods and multilinear models.

GEORG PANGALOS received the Dipl.-Ing. degree in electrical engineering and the Ph.D. degree in control engineering from the Hamburg University of Technology, in 2011 and 2015, respectively.

Since 2015, he has been working at the Fraunhofer-Gesellschaft zur Förderung der angewandten Forschung e.V., Hamburg, Germany. His research interests include the areas of renewable energy integration and energy systems transition.

JAVIER SANCHIS SÁEZ received the B.Sc. and Ph.D. degrees in computer science from Universitat Politècnica de València, Spain, in 1993 and 2002, respectively.

He is a Professor with the Department of Systems Engineering and Control, Universitat Politècnica de València. He has more than 15 years of experience applying soft computing methods to engineering problems related with process control and optimization. His main research interests include multivariable predictive control, constrained process control and computational intelligence methods for systems engineering, and process control.